SCIENCE CHINA
Chemistry

•ARTICLES•

https://doi.org/10.1007/s11426-024-2341-8

A hybrid ZnO nanoparticle electron transporting layer for inverted structure organic solar cells with efficiency over 19%

Xin Chen, Jian Liu, Zheng Xiao, Zhaochen Suo, Jie Wang, Zhaoyang Yao, Chenxi Li, Xiangjian Wan* & Yongsheng Chen

State Key Laboratory of Elemento-Organic Chemistry, Center for New Organic Matter, The Centre of Nanoscale Science and Technology and Key Laboratory of Functional Polymer Materials, Renewable Energy Conversion and Storage Center (RECAST), Tianjin Key Laboratory of Functional Polymer Materials, College of Chemistry, Nankai University, Tianjin 300071, China

Received August 2, 2024; accepted September 30, 2024; published online November 4, 2024

Electron transport layers (ETLs) play a pivotal role in determining the efficiency and stability of inverted structure organic solar cells (OSCs). Zinc oxide nanoparticles (ZnO NPs) are commonly used as ETLs due to their mild deposition conditions and compatibility with flexible plastic substrates, facilitating scalable manufacturing. In this study, we introduce a molecule called NMO, which serves a dual purpose: efficiently dispersing ZnO nanoparticles and acting as a surface modification layer for ZnO NPs thin films. The hybrid ETL created by blending and surface modification with NMO significantly enhances both the efficiency and stability of OSCs. Inverted structure OSCs, based on the PM6:Y6 system and utilizing the hybrid ETL, achieve impressive power conversion efficiency (PCE) of 18.31%. Moreover, these devices demonstrate exceptional stability during shelf storage (T_{80} = 19,650 h), thermal aging (T_{80} = 7783 h), and maximum power point tracking (T_{80} = 3009 h). Importantly, the hybrid ETL exhibits good generality, as all tested OSCs utilizing it display significantly improved efficiencies and stabilities. Notably, a PCE of 19.23% is attained for the PM6:BTP-eC9-based device, marking the highest reported efficiency for inverted single-junction OSCs to date.

organic solar cells, interface layers, ZnO nanoparticles, stability, efficiency

Citation: Chen X, Liu J, Xiao Z, Suo Z, Wang J, Yao Z, Li C, Wan X, Chen Y. A hybrid ZnO nanoparticle electron transporting layer for inverted structure organic solar cells with efficiency over 19%. *Sci China Chem*, 2024, 67, https://doi.org/10.1007/s11426-024-2341-8

1 Introduction

With the advantages of flexibility, low cost, and large-area printing, organic solar cells (OSCs) have broad application prospects in building integration, wearable electronic devices, and other fields [1–5]. In recent years, there has been a rapid increase in the power conversion efficiencies (PCEs) of OSCs, surpassing 20% [6–9]. However, achieving both high efficiency and stability remains a formidable challenge, essential for the commercialization of OSCs [10–13]. Typically, OSCs with an inverted architecture offer improved stability and compatibility with roll-to-roll printing. However, their efficiencies are generally lower than those of devices with a normal structure [14–16]. This underscores the pressing need to develop inverted OSCs with high performance and stability. The electron transport layers (ETLs) play a pivotal role in fabricating inverted structure devices. Among commonly used ETLs, zinc oxide (ZnO), especially when prepared via the sol-gel method, has found widespread use in inverted OSCs due to its high electron mobility and straightforward preparation [17,18]. Nevertheless, the high-temperature (usually 200°C) post-treatment required for sol-gel ZnO significantly hinders its application in flexible devices and roll-to-roll OSCs manufacturing. Furthermore,

*Corresponding author (email: xjwan@nankai.edu.cn)

ZnO exhibits a photocatalytic effect that compromises device photo-stability [19,20]. ZnO nanoparticles (ZnO NPs) offer the advantage of being easily prepared and treated at lower temperatures. However, OSCs based on ZnO NPs typically exhibit lower efficiencies than those using sol-gel ZnO, primarily due to the presence of surface defects [21–25]. Additionally, ZnO NPs tend to aggregate in processing solutions, leading to inferior device performance. Numerous efforts have been made to address these ZnO-related challenges, particularly through surface modification, but the results have fallen short of achieving satisfactory OSC performance in terms of efficiency and stability, especially when mild processing conditions are used with ZnO NPs as the ETL [14,26–30].

In this study, we have designed and synthesized a molecule named NMO. It can anchor onto ZnO NPs and effectively prevent their aggregation in alcohol solution. Importantly, through blending and film surface modification with NMO, the work function, conductivity, and interfacial properties of ZnO NPs based film can be substantially optimized. As a result, utilizing the hybrid ETL composed of ZnO NPs and NMO, the typical PM6:Y6-based device achieves an impressive efficiency of 18.31% and exceptional stability during shelf storage (T_{80} = 19650 h), thermal aging (T_{80} = 7783 h), and maximum power point (MPP) tracking (T_{80} = 3009 h). Notably, this hybrid ETL exhibits good generality, as all tested OSCs employing it demonstrate significantly improved efficiencies and stabilities compared to control devices. Particularly noteworthy is the attainment of a PCE of 19.23% for the PM6:BTP-eC9 system, marking the highest reported efficiency for inverted single-junction OSCs to date [10,11,15,25,31–41].

2 Results and discussion

The chemical structure of NMO is depicted in Figure 1a. It can be readily synthesized in a single step using commercially available reagents. The detailed synthesis procedure is provided in the supporting information. NMO features alkoxy chains, allowing it to dissolve easily in alcohol solvents such as methanol and ethanol. Importantly, it does not dissolve in halogen solvents like chloroform and chlorobenzene, which are commonly used as solvents for active layer materials. This property makes it suitable for use as a modified layer on ZnO films. As illustrated in Figure 1a, ZnO NPs in methanol form a white cloudy solution. However, after adding NMO at a weight ratio of 15% compared to ZnO NPs, the solution becomes transparent. Dynamic light scattering (DLS) measurement (Figure 1b) shows that the addition of NMO effectively disperses ZnO NPs in the methanol solution. Even after 70 days, the size distribution of ZnO NPs with NMO remains unchanged in the blended solution (10 ± 1 nm). In contrast, the control ZnO NPs without NMO aggregate into clusters, leading to a significant increase in particle diameters from 23 to 120 nm. The effective and stable dispersion of ZnO NPs with NMO is primarily attributed to the strong interaction between the carboxyl acid groups on NMO and the hydroxide groups of ZnO NPs. As revealed in the Fourier transform infrared spectroscopy (FTIR) spectra (Figure 1c), the vibrational peaks of the C=O group in NMO shift from 1700 to 1615 cm^{-1}, and simultaneously, the hydroxyl (O–H) vibration peak of NMO disappears in the NMO and ZnO NPs blend. In this study, we refer to the blend of ZnO NPs and NMO as ZnO:NMO. These results indicate that the carboxyl groups on NMO chemically passivate ZnO NPs. Furthermore, X-ray photoelectron spectroscopy (XPS) characterization was performed on the films of bare ZnO NPs and ZnO: NMO. As shown in Figure 1d–f, clear C=C and COO^- peaks originating from the NMO molecule are observed at binding energies of 285.9 and 288.1 eV, respectively, in the film of ZnO: NMO [42]. Meanwhile, the Zn 2p peaks at 1044.7 and 1021.6 eV shift towards lower energy both by 0.2 eV. Moreover, after blending with NMO, the signal of lattice oxygen in ZnO remains unchanged. However, the peak corresponding to defect oxygen, including oxygen vacancies and oxygen adsorbed on the surface of ZnO NPs, shifts from 531.7 to 531.9 eV. Importantly, the peak intensity of lattice oxygen increases while that of defect oxygen decreases. The ratio of lattice oxygen to defect oxygen changes from 0.25 to 3.17 before and after modification, calculated from the corresponding peak areas. These findings indicate a significant reduction in oxygen defects in ZnO NPs after blending with NMO.

To assess the potential of ZnO:NMO as an ETL, we fabricated OSCs with an inverted structure of ITO/ETL/Active layer/MoOx/Ag. The device architecture is illustrated in Figure 2a. We chose PM6:Y6, a representative OSC system, as the active layer. After optimization, the device employing ZnO:NMO as the ETL achieved an efficiency of 16.53%, surpassing that of the control device using bare ZnO NPs (15.50%). Remarkably, when the ZnO:NMO film was further surface-modified with NMO (ZnO:NMO/NMO) and used as the ETL, the device exhibited an impressive PCE of 18.31%, marking the highest efficiency reported for PM6:Y6-based inverted OSCs to date. The optimized photovoltaic parameters are summarized in Table 1, and the corresponding *J-V* and EQE curves are displayed in Figure 2b and c. It is worth noting that surface modification with NMO on bare ZnO NPs or sol-gel ZnO had a modest, though not significant, effect on improving device efficiencies compared to control devices (Figure S6, Table S1). These results suggest that the combination of ZnO NPs dispersion and film surface modification played a crucial role in enhancing device performance.

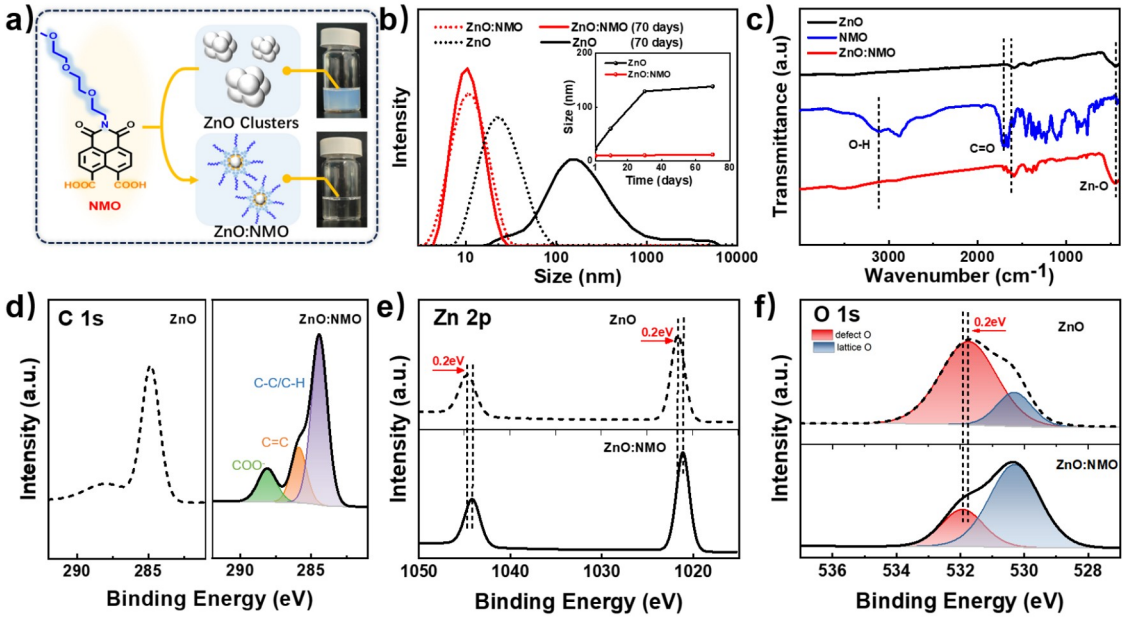

Figure 1 (Color online) (a) Chemical structure of NMO, and photo images of ZnO NPs with and without NMO (15%wt). (b) DLS measurement results, where the insert is the size change with time. (c) FTIR spectra of ZnO NPs, NMO and their blending film. (d–f) XPS of ZnO NPs with and without NMO.

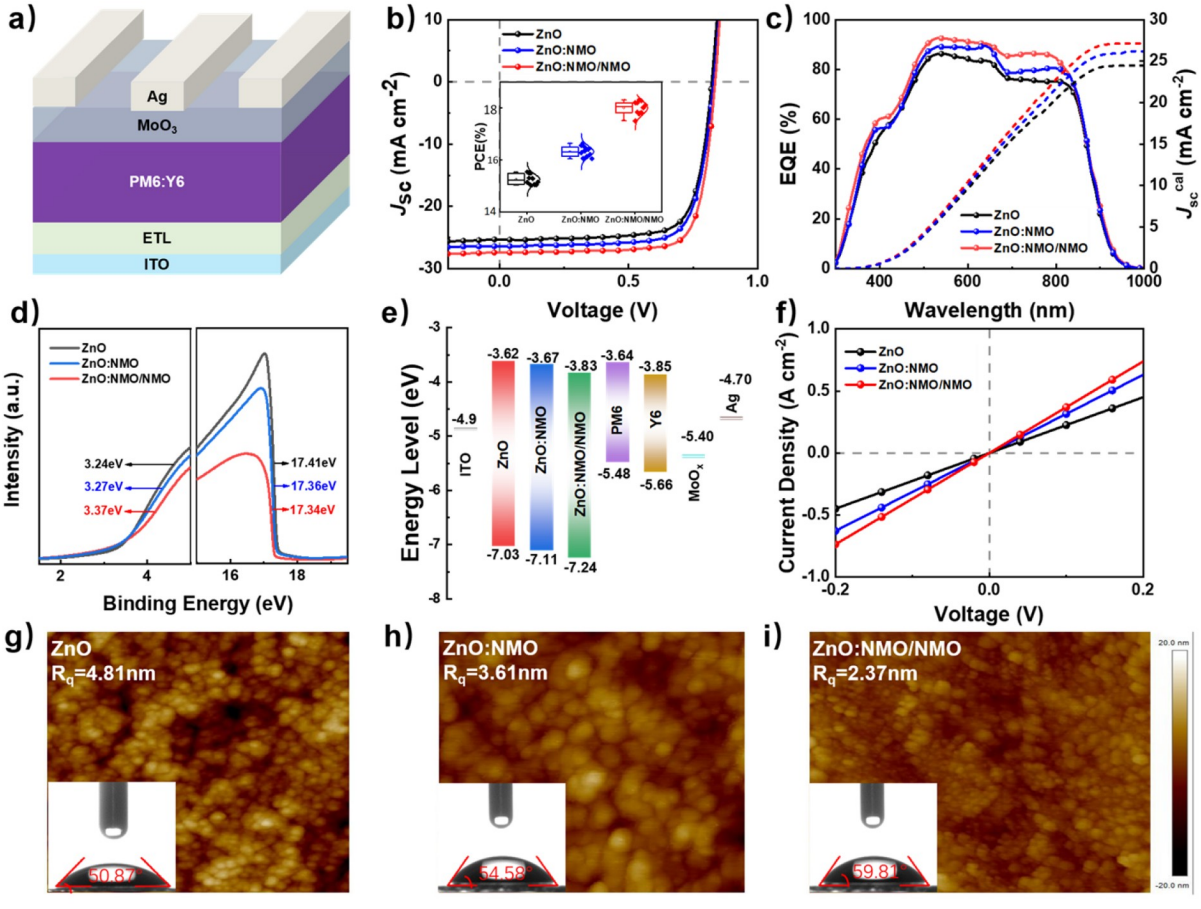

Figure 2 (Color online) (a) Photovoltaic device architecture in this work. (b) *J-V* curves. (c) EQE spectra. (d) UPS characterizations of the three films. (e) Energy levels of ITO, ZnO NPs, ZnO:NMO, ZnO:NMO/NMO, PM6, Y6, MoOx, and Ag. (f) Conductivity measurement *J-V* curves of the three films. (g–i) Atomic force microscopy (AFM) height images of the films of ZnO NPs, ZnO:NMO and ZnO:NMO/NMO, the inserts are the contact angle measurement results on water.

Table 1 Optimized photovoltaic parameters of the PM6:Y6 based devices with different ETLs[a)]

ETL	V_{oc} [V]	J_{sc} [mA cm^{-2}]	J_{sc}^{cal} [mA cm^{-2}][b)]	FF [%]	PCE [%]
ZnO NPs	0.824	25.11	24.80	74.68	15.50
	(0.822 ± 0.002)	(24.71 ± 0.46)		(74.82 ± 0.90)	(15.26 ± 0.19)
ZnO:NMO[c)]	0.829	26.40	25.95	75.45	16.53
	(0.827 ± 0.003)	(26.21 ± 0.33)		(75.37 ± 0.27)	(16.32 ± 0.21)
ZnO:NMO/NMO[d)]	0.846	27.65	27.14	78.08	18.31
	(0.844 ± 0.003)	(27.47 ± 0.29)		(77.70 ± 0.63)	(18.01 ± 0.26)

a) Optimal results and statistical results are listed outside of parentheses and in parentheses, respectively. The average parameters were calculated from 10 independent devices. b) Integrated short-circuit current (J_{sc}) from EQE curve. c) ZnO NPs blended with NMO. d) ZnO NPs blended with NMO and then the corresponding film modified with NMO.

To understand the mechanism responsible for the enhanced device performance using the hybrid ETL ZnO:NMO/NMO, we conducted ultraviolet photoelectron spectroscopy (UPS) measurements on films of ZnO NPs, ZnO:NMO, and ZnO:NMO/NMO. From the secondary electron cutoff (E_{cutoff}) edges (Figure 2d), we determined the work functions (WF) of these films to be 3.79, 3.84, and 3.86 eV, respectively. The valence band maximum (VBM) values calculated from the Fermi level and the highest occupied state (HOS) were −7.03, −7.11, and −7.24 for ZnO NPs, ZnO:NMO, and ZnO:NMO/NMO, respectively. To estimate the conduction band minimum (CBM), we used the VBM and optical bandgap, resulting in values of −3.62, −3.67, and −3.83 eV for ZnO NPs, ZnO:NMO, and ZnO:NMO/NMO films. As illustrated in Figure 2e, ZnO:NMO/NMO films exhibited the shallowest energy levels, minimizing interfacial barriers between the active layer film and the electrode, thereby facilitating charge extraction and carrier transport in inverted devices [14,21]. We measured the conductivity of the three films using the device structure ITO/ETL/Ag (Figure 2f). Calculated from the slope of the *J-V* curves, the conductivity of ZnO NPs, ZnO:NMO, and ZnO:NMO/NMO films were determined to be 8.76×10^{-4}, 9.44×10^{-4}, and 1.14×10^{-3} S cm^{-1}, respectively. The enhanced conductivity of ZnO:NMO and ZnO:NMO/NMO films suggests fewer surface defects in ZnO NPs and reduced series resistance, which benefits the improvement of the device fill factor (FF).

In addition to tuning the work function and conductivity properties, ETLs can influence the morphology of bulk heterojunction active layers, as the surface properties initiate the morphological framework. To investigate this, we analyzed the surface properties of bare ZnO NPs, ZnO:NMO, and ZnO:NMO/NMO films. As depicted in Figure 2g–i, the ZnO:NMO/NMO film displayed a smoother and more uniform surface with a root-mean-square roughness (R_q) of 2.37 nm, compared to the roughness of bare ZnO NPs (4.81 nm) and ZnO:NMO (3.61 nm) films, and NMO is evenly distributed on the ZnO:NMO surface from the energy dispersive X-ray spectroscopy (EDS) measurement (Figure S7). Furthermore, we tested the contact angles of these films with water and glycerol and calculated surface tension (γ_s) values following Wu's model [43]. The results in Table S2 show that bare ZnO NPs and ZnO:NMO films had similar γ_s with values of 63.8 and 62.1 mJ m^{-2}, respectively. In contrast, the ZnO:NMO/NMO film exhibited a lower γ_s of 53.3 mJ m^{-2}. PM6 and Y6 had γ_s values of 27.5 and 29.3 mJ m^{-2}, respectively, under the same conditions. The reduced γ_s of the hybrid ETL ZnO:NMO/NMO is beneficial for Y6 aggregation near the ETL, facilitating charge transport in inverted structure OSCs. To confirm this assumption, we investigated the vertical phase distribution of the active layer in devices using bare ZnO NPs and the hybrid ETL ZnO:NMO/NMO through time-of-flight secondary ion mass spectrometry (TOF-SIMS). CN^- serves as an indicator of Y6, while F^- represents the total component of PM6 and Y6. The ratio of CN^- intensity to F^- intensity partially represents the amount of Y6 at a specific location/height in the vertical direction [44,45]. As shown in Figure S8, a higher CN^-/F^- ratio was observed in the region near the bottom ETL (1.32 vs. 2.73), indicating that more Y6 was accumulated near the cathode in the hybrid ETL-based device, consistent with the surface energy analysis results mentioned earlier.

To gain a deeper understanding of the enhanced performance of devices utilizing the hybrid ETL ZnO:NMO/NMO, dynamic measurements were conducted to investigate the exciton dissociation process, charge transport properties, and recombination. Firstly, we measured the dependence of photocurrent density (J_{ph}) on effective voltage (V_{eff}) for both devices (Figure 3a). The exciton dissociation probability (P_{diss}) was calculated by dividing J_{ph} by the saturated photocurrent density (J_{sat}). Under short-circuit current and maximal power point conditions, the control and hybrid ETL-based devices exhibited P_{diss} values of 95.8% vs. 97.7%, and 79.5% vs. 89.5%, respectively. The larger P_{diss} values in the hybrid ETL-based device indicate a more effective exciton dissociation process compared to the control device. We also employed transient photocurrent (TPC) and transient photovoltage (TPV) characterizations to investigate

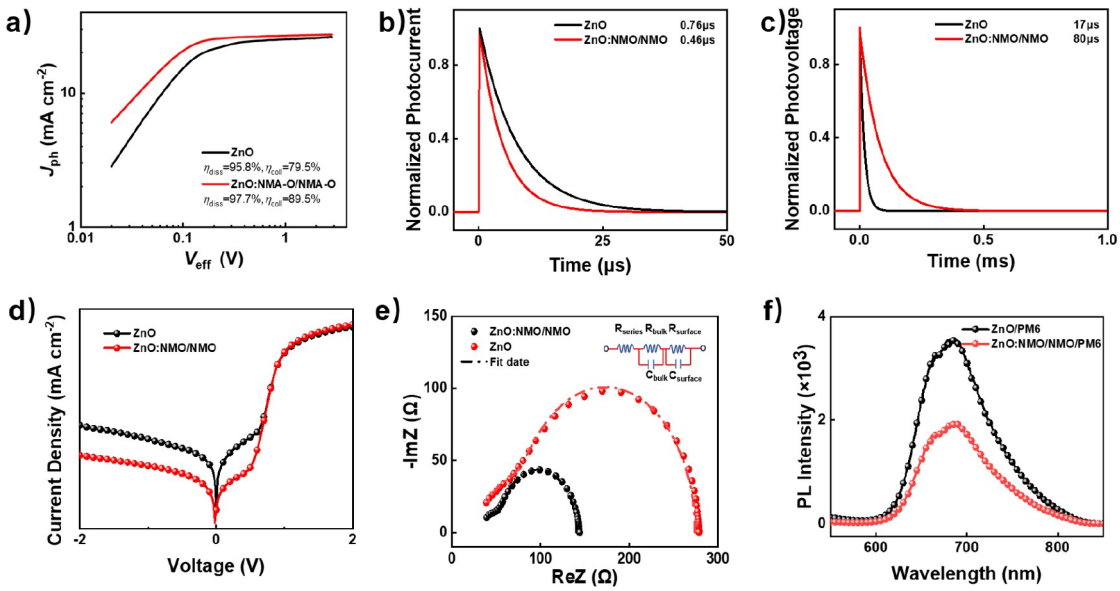

Figure 3 (Color online) (a) Photocurrent density versus effective voltage (J_{ph}-V_{eff}) characteristics for the devices based on ZnO NPs and ZnO:NMO/NMO. (b) Transient photocurrent and (c) transient photovoltage measurements of devices based on ZnO NPs and ZnO:NMO/NMO. (d) *J*-*V* characteristics in the dark of devices based on ZnO NPs and ZnO:NMO/NMO. (e) Nyquist plots of devices. (f) PL spectra of PM6 spin-coated films on the ZnO NPs and ZnO:NMO/NMO layer under 400 nm excitation.

charge extraction and recombination properties (Figure 3b and c). In comparison to the control device, the hybrid ETL-based device displayed a shorter charge extraction time (0.46 μs vs. 0.76 μs) and a significantly longer carrier lifetime (80 μs vs. 17 μs). These results suggest that the hybrid ETL effectively improves charge extraction efficiency and transport in inverted devices, which aligns with the observed enhancements in FF and J_{sc}. Furthermore, we examined the *J*-*V* curves of the control and hybrid ETL-based devices under dark conditions (Figure 3d). The device with the hybrid ETL demonstrated reduced leakage current under reverse bias voltage and an enhanced rectification ratio when compared to the control device. These findings indicate a more efficient carrier injection process. To study the interface resistances of the two devices, we conducted electrochemical impedance spectroscopy (EIS) measurements (Figure 3e). The hybrid ETL-based device exhibited series and surface resistances of 33.6 and 19.4 Ω, respectively, which were lower than those of the device based solely on bare ZnO NPs, which had values of 35.2 and 44.0 Ω, respectively. The reduced values of series resistance (R_{series}) and surface resistance ($R_{surface}$) signify fewer interfacial defects and improved contact between the active layer and ETL, favorably suppressing interfacial charge recombination and enhancing charge extraction. In addition, the photoluminescence (PL) spectra of PM6 spin-coated on the ZnO NPs and ZnO:NMO/NMO films are shown in Figure 3f. The PL of PM6 was substantially quenched on the ZnO:NMO/NMO film, indicating more efficient exciton dissociation and electron extraction from the donor to the hybrid ETL. Moreover, the excellent electron transport and extraction capabilities of ZnO:NMO/NMO ETL guarantee its layer thickness can be adjusted in the large range (from 20 to 50 nm), without significantly affecting device performance (Table S3).

Achieving long-term stability remains a significant challenge for OSCs. In inverted structure OSCs, which commonly employ sol-gel and nanoparticle ZnO as ETLs, the issue of photoinduced catalysis poses a serious threat to OSCs stability. Despite substantial efforts dedicated to addressing this problem, it remains a challenge to simultaneously achieve high efficiency and good stability in inverted OSCs using ZnO-based ETLs. To assess the impact of the hybrid ETL ZnO:NMO/NMO on device stability, we conducted measurements involving shelf storage, thermal aging, and operation at the MPP for devices utilizing the hybrid ETL compared to those using bare ZnO NPs. As depicted in Figure 4a, the PM6:Y6 device employing the hybrid ETL demonstrated outstanding shelf stability, with the efficiency of the leading device remaining at 99.5% after 1000 h of storage in a glove box filled with N_2. The champion device exhibited a fitting T_{80} of 19,650 h, significantly higher than that of the device based on bare ZnO NPs, which had a T_{80} of 2628 h. Moreover, the device utilizing the hybrid ETL displayed commendable thermal stability. As shown in Figure 4b, the power conversion efficiency (PCE) of the PM6:Y6 device with the hybrid ETL retained 96.6% of its initial value after 1000 h of thermal treatment at 65°C, with a T_{80} of 7783 h. In contrast, the PCE of the bare ZnO NPs-based device dropped to 87.9% of its initial efficiency, with a T_{80} of 1481 h. Crucially, we also evaluated the light stability of the device operating at the MPP under continuous illu-

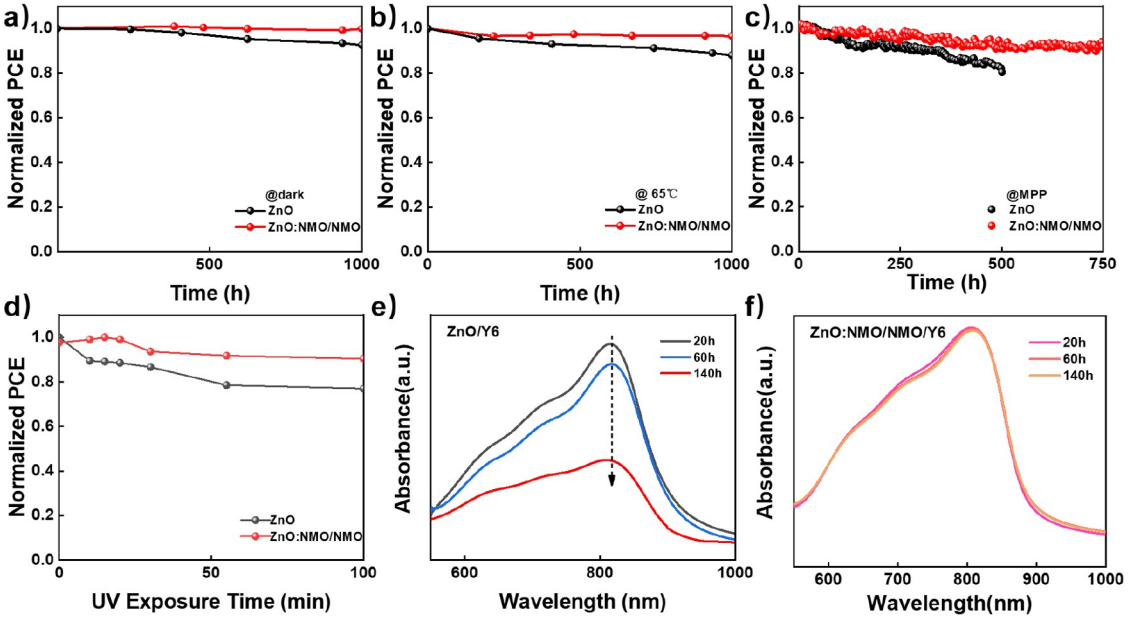

Figure 4 (Color online) The photovoltaic properties of OSCs based on PM6:Y6 active layer with ZnO NPs and ZnO:NMO/NMO as ETL. (a) Shelf storage stability test, (b) thermal aging stability test at 65°C in N_2 atmosphere. (c) Operational stability test at MPP tracking with continuous illumination of 100 mW cm^{-2} provided by LED arrays at 25°C in N_2 atmosphere. (d) Devices stability test under continuous UV illumination. (e) UV-visible (UV-vis) absorption spectra of Y6 film coated on the substrate glass/ZnO NPs, and (f) glass/ZnO:NMO/NMO with different exposing times under continuous UV illumination in ambient conditions.

mination from a 100 mW cm^{-2} LED. As depicted in Figure 4c, the device employing the hybrid ETL exhibited robust photostability, retaining 92.1 % of its initial efficiency after 750 h of continuous illumination, with a T_{80} of 3009 h. Conversely, the efficiency of the device with bare ZnO NPs decreased to 80% of its initial efficiency, with a T_{80} of 497 h. We further investigate the photostability of the devices with the hybrid ETL and bare ZnO NPs under extreme conditions, i.e., continuous ultraviolet (UV) irradiation (365 nm, 40 mW cm^{-2}). As shown in Figure 4d, after 100 min exposure to UV exposure, the hybrid ETL-based device maintains 90.4 % of its initial efficiency. While the bare ZnO NPs based device only maintains 80% of the initial PCE. As shown in Figure 4e and f, under continuous UV illumination, the absorption strength of Y6 film coated on glass/ZnO NPs significantly decreased after 140 h. In contrast, there is nearly no change in the absorption of Y6 film coated on the glass/ZnO:NMO/NMO hybrid film, which indicates rather good stability of Y6 film owing to much reduced photocatalytic of the hybrid ETL.

To assess the generality of the hybrid ETL ZnO:NMO/NMO, we fabricated inverted structure OSCs using other typical active layer systems. The chemical structures of the donor and acceptor materials are provided in Figure S9. As summarized in Table 2, the use of the hybrid ETL led to a significant enhancement in the efficiencies of all the devices. Notably, the device based on PM6:BTP-eC9 achieved a PCE of 19.23%, marking the highest reported efficiency to date for inverted structure OSCs (Table S5). Additionally, all of these devices demonstrated considerable stability when operated at MPP tracking compared to the control devices employing bare ZnO NPs (Figures S11 and S12). On the other hand, the conventional thermal annealing process for sol-gel ZnO at temperatures ranging from 150–200°C imposes a significant constraint on its use in flexible OSCs. This limitation arises because common flexible substrates, such as polyethylene terephthalate (PET) and polyethylene naphthalate (PEN), cannot endure such high-temperature treatments. However, it is noteworthy that the hybrid ETL ZnO:NMO/NMO, when treated at mild or even ambient temperatures, still delivers exceptional device performance for typical PM6:Y6-based devices. Table S4 presents the performance of PM6:Y6 devices based on the hybrid ETL subjected to various thermal annealing temperatures. Remarkably, a PCE of 17.87% was achieved in the as-cast condition, only slightly lower than the devices annealed at 120°C. To validate this concept, we fabricated the flexible OSC based on PM6:Y6, employing an indium tin oxide-coated polyethylene naphthalate (PEN/ITO) film as the transparent electrode, achieving a PCE of 17.14% (Figure S14). This result stands among the best reported results for flexible OSCs based on PM6:Y6 to date [15,46–50].

3 Conclusions

In summary, we have developed a modified molecule called NMO, which serves a dual role in efficiently dispersing ZnO

Table 2 Optimized photovoltaic parameters of different active layer based inverted structure devices with bare ZnO NPs and ZnO:NMO/NMO[a)]

Active layer	ETL	V_{oc} [V]	J_{sc} [mA cm^{-2}]	J_{sc}^{cal} [mA cm^{-2}][b)]	FF [%]	PCE [%]
PM6:L8-BO	ZnO	0.871	25.16	25.06	78.89	17.29 (17.02 ± 0.09)
	ZnO:NMO/NMO[c)]	0.878	26.50	25.75	78.90	18.35 (18.17 ± 0.06)
PM6:CH23	ZnO	0.874	25.94	24.93	75.89	17.18 (17.01 ± 0.09)
	ZnO:NMO/NMO	0.876	26.68	25.95	78.43	18.33 (18.17 ± 0.13)
D18:N3	ZnO	0.844	25.68	24.79	76.32	16.48 (15.98 ± 0.37)
	ZnO:NMO/NMO	0.856	27.88	26.54	77.03	18.30 (18.11 ± 0.33)
PM6:F-2Cl	ZnO	0.890	18.20	17.79	76.55	12.44 (12.35 ± 0.16)
	ZnO:NMO/NMO	0.891	19.65	18.67	76.55	13.59 (13.49 ± 0.19)
PM6:BO-4Cl	ZnO	0.830	25.86	25.06	77.73	16.68 (16.53 ± 0.17)
	ZnO:NMO/NMO	0.836	27.58	26.53	78.51	18.12 (18.05 ± 0.18)
PM6:BTP-eC9	ZnO	0.848	26.98	26.37	76.13	17.49 (17.24 ± 0.17)
	ZnO:NMO/NMO	0.858	28.24	27.46	79.32	19.23 (19.09 ± 0.12)

a) Optimal results and statistical results are listed outside of parentheses and in parentheses, respectively. The average parameters were calculated from 10 independent devices. b) Integrated J_{sc} from EQE curve. c) ZnO NPs blended with NMO and then the corresponding film modified with NMO.

NPs and acting as a surface modification layer for thin films. The hybrid ETL created by blending and surface modification with NMO significantly enhances device efficiency and stability. Using PM6:Y6 as a representative model system, our inverted OSC with the hybrid ETL achieved an impressive PCE of 18.31%. Moreover, this device demonstrated exceptional stability during shelf storage (T_{80} = 19,650 h), thermal aging (T_{80} = 7783 h), and MPP tracking (T_{80} = 3009 h). The key factors contributing to the improved device performance include: (i) reduced energy barriers, enhanced conductivity, improved charge extraction, and reduced charge accumulation and recombination; (ii) diminished levels of defect oxygen on the surface of ZnO NPs, thereby suppressing ZnO's photocatalytic activity; (iii) optimized vertical phase separation in the active layer due to reduced surface energy. Furthermore, the generality of the hybrid ETL was demonstrated by its ability to enhance the efficiency and stability of other active layer systems in inverted devices. Particularly noteworthy is the achievement of a remarkable PCE of 19.23% for the PM6:BTP-eC9 system, marking the highest reported efficiency to date for single-junction inverted structure OSCs. Importantly, as the ZnO NPs-based hybrid ETL does not require high-temperature treatment, it is compatible with common flexible substrates, making it suitable for the roll-to-roll production of OSCs. Overall, this research presents an efficient ETL approach that holds promise for achieving high efficiency, stability, and compatibility in future commercial OSC manufacturing.

Acknowledgements This work was supported by the National Natural Science Foundation of China (NSFC) (52025033, 52373189 and 21935007) and Ministry of Science and Technology of the People's Republic of China (MoST) (2019YFA0705900, 2022YFB4200400 and 2023YFE0210400).

Conflict of interest The authors declare no conflict of interest.

Supporting information The supporting information is available online at chem.scichina.com and link.springer.com/journal/11426. The supporting materials are published as submitted, without typesetting or editing. The responsibility for scientific accuracy and content remains entirely with the authors.

1 Mazzio KA, Luscombe CK. *Chem Soc Rev*, 2015, 44: 78–90
2 Wan X, Li C, Zhang M, Chen Y. *Chem Soc Rev*, 2020, 49: 2828–2842
3 Zhang G, Lin FR, Qi F, Heumüller T, Distler A, Egelhaaf HJ, Li N, Chow PCY, Brabec CJ, Jen AKY, Yip HL. *Chem Rev*, 2022, 122: 14180–14274
4 Li S, Li Z, Wan X, Chen Y. *eScience*, 2023, 3: 100085
5 Wei Q, Liu W, Leclerc M, Yuan J, Chen H, Zou Y. *Sci China Chem*, 2020, 63: 1352–1366
6 Chen Z, Ge J, Song W, Tong X, Liu H, Yu X, Li J, Shi J, Xie L, Han

C, Liu Q, Ge Z. *Adv Mater*, 2024, 36: 2406690
7 Guan S, Li Y, Xu C, Yin N, Xu C, Wang C, Wang M, Xu Y, Chen Q, Wang D, Zuo L, Chen H. *Adv Mater*, 2024, 36: 2400342
8 Lu H, Li D, Liu W, Ran G, Wu H, Wei N, Tang Z, Liu Y, Zhang W, Bo Z. *Angew Chem Int Ed*, 2024, 63: e202407007
9 Jiang Y, Sun S, Xu R, Liu F, Miao X, Ran G, Liu K, Yi Y, Zhang W, Zhu X. *Nat Energy*, 2024, 9: 975–986
10 Li ST, Fu Q, Meng LX, Wan XJ, Ding LM, Lu GY, Lu GH, Yao ZY, Li CX, Chen YS. *Angew Chem Int Ed*, 2022, 61: 2306095
11 Yu Y, Cui Y, Zhang T, Chen ZH, Xiao Y, Wang WX, Yang Y, Yang N, Hou JH. *Adv Funct Mater*, 2023, 33: 2306095
12 Dennler G, Scharber MC, Brabec CJ. *Adv Mater*, 2009, 21: 1323–1338
13 Wang H, Wu S, Yang D, Yu X, Yang S, Ding P, Yan P, Ma Z, Zhang J, Ge Z. *Sci China Chem*, 2024, 67: 2686–2693
14 Liu H, Liu ZX, Wang S, Huang J, Ju H, Chen Q, Yu J, Chen H, Li CZ. *Adv Energy Mater*, 2019, 9: 1900887
15 Liu X, Zheng Z, Wang J, Wang Y, Xu B, Zhang S, Hou J. *Adv Mater*, 2022, 34: 2106453
16 Yip HL, Hau SK, Baek NS, Ma H, Jen AKY. *Adv Mater*, 2008, 20: 2376–2382
17 Huang J, Yin Z, Zheng Q. *Energy Environ Sci*, 2011, 4: 3861–3877
18 Tang HR, Bai YQ, Zhao HY, Qin XD, Hu ZC, Zhou C, Huang F, Cao Y. *Adv Mater*, 2024, 36: 2212236.
19 Luke J, Corrêa L, Rodrigues J, Martins J, Daboczi M, Bagnis D, Kim J. *Adv Energy Mater*, 2021, 11: 2003405
20 Trost S, Zilberberg K, Behrendt A, Polywka A, Görrn P, Reckers P, Maibach J, Mayer T, Riedl T. *Adv Energy Mater*, 2013, 3: 1437–1444
21 Tao Y, Liu H, Wang D, Zhao F, Chen Z, Zhu H, Chen H, Li CZ. *InfoMat*, 2022, 4: e12276
22 Chen S, Manders JR, Tsang SW, So F. *J Mater Chem*, 2012, 22: 24202–24212
23 Li S, Xiao Z, Li JJ, Hu ZY, Yang Y, Kan B, Guo DS, Wan X, Yao Z, Li C, Chen Y. *Sci China Chem*, 2023, 66: 195–201
24 Liu C, Xiao C, Li W. *J Mater Chem C*, 2021, 9: 14093–14114
25 Wang Y, Zheng Z, Wang J, Liu X, Ren J, An C, Zhang S, Hou J. *Adv Mater*, 2023, 35: 2208305
26 Byeon H, Kim B, Hwang H, Kim M, Yoo H, Song H, Lee SH, Lee BH. *ACS Appl Mater Interfaces*, 2023, 15: 10926–10935
27 Fan P, Zhang D, Wu Y, Yu J, Russell TP. *Adv Funct Mater*, 2020, 30: 2002932
28 Li CZ, Huang J, Ju H, Zang Y, Zhang J, Zhu J, Chen H, Jen AKY. *Adv Mater*, 2016, 28: 7269–7275
29 Wang ZG, Guo JB, Pan YQ, Fang J, Gong C, Mo LX, Luo Q, Lin J, Ma CQ. *Energy Environ Mater*, 2023, 7: e12592
30 Yu H, Huang X, Huang C. *Appl Surf Sci*, 2019, 470: 318–330
31 Abbas Z, Ryu SU, Haris M, Song CE, Lee HK, Lee SK, Shin WS, Park T, Lee JC. *Nano Energy*, 2022, 101: 107574
32 Dong Y, Yu R, Zhao B, Gong Y, Jia H, Ma Z, Gao H, Tan Z. *ACS Appl Mater Interfaces*, 2022, 14: 1280–1289
33 Han Y, Dong H, Pan W, Liu B, Chen X, Huang R, Li Z, Li F, Luo Q, Zhang J, Wei Z, Ma CQ. *ACS Appl Mater Interfaces*, 2021, 13: 17869–17881
34 Huang Q, Jing J, Zhang K, Chen Y, Song A, Liu Z, Huang F. *J Mater Chem A*, 2022, 10: 23973–23981
35 Jiang Y, Dong X, Sun L, Liu T, Qin F, Xie C, Jiang P, Hu L, Lu X, Zhou X, Meng W, Li N, Brabec CJ, Zhou Y. *Nat Energy*, 2022, 7: 352–359
36 Li C, Zhou J, Song J, Xu J, Zhang H, Zhang X, Guo J, Zhu L, Wei D, Han G, Min J, Zhang Y, Xie Z, Yi Y, Yan H, Gao F, Liu F, Sun Y. *Nat Energy*, 2021, 6: 605–613
37 Lin Y, Zhang Y, Magomedov A, Gkogkosi E, Zhang J, Zheng X, El-Labban A, Barlow S, Getautis V, Wang E, Tsetseris L, Marder SR, McCulloch I, Anthopoulos TD. *Mater Horiz*, 2023, 10: 1292–1300
38 Yang S, Yu H. *Chem Eng J*, 2023, 452: 139658
39 Yang Y, Xiao Y, Xu B, Hou J. *Adv Energy Mater*, 2023, 13: 2301098
40 Yu R, Shi R, Liu H, Wu G, Ma Z, Gao H, He Z, Tan Z. *Adv Energy Mater*, 2022, 12: 2201306
41 Yu R, Wei X, Wu G, Zhang T, Gong Y, Zhao B, Hou J, Yang C, Tan Z. *Energy Environ Sci*, 2022, 15: 822–829
42 Smecca E, Motta A, Fragalà ME, Aleeva Y, Condorelli GG. *J Phys Chem C*, 2013, 117: 5364–5372
43 Comyn J. *Int J Adhes Adhes*, 1992, 12: 145–149
44 Zhan LL, Li SX, Xia XX, Li YK, Lu XH, Zuo LJ, Shi MM, Chen HZ. *Adv Mater*, 2021, 33: 2007231
45 Zhang X, Li Y, Zhang D, Wu G, Zhang H, Zhou J, Li X, Saud-uz-Zafar X, Zhang J, Wei Z, Zhou H, Zhang Y. *Sci China Chem*, 2021, 64: 116–126
46 Chen Z, Song W, Yu K, Ge J, Zhang J, Xie L, Peng R, Ge Z. *Joule*, 2021, 5: 2395–2407
47 Lee JW, Sun C, Lee C, Tan Z, Phan TNL, Jeon H, Jeong D, Kwon SK, Kim YH, Kim BJ. *ACS Energy Lett*, 2023, 8: 1344–1353
48 Song W, Fan X, Xu B, Yan F, Cui H, Wei Q, Peng R, Hong L, Huang J, Ge Z. *Adv Mater*, 2018, 30: 1800075
49 Song W, Ye QR, Yang SC, Xie L, Meng YY, Chen ZY, Gu Q, Yang DB, Shi JY, Ge ZY. *Angew Chem Int Ed*, 2023, 62: e202310034
50 Song W, Yu K, Ge J, Xie L, Zhou R, Peng R, Zhang X, Yang M, Wei Z, Ge Z. *Matter*, 2022, 5: 1877–1889